Supporting Information

For **Surface Roughness: A Crucial Factor to Robust Electric Double Layer Capacitors**

By *Jishi Wei,*[a] Yongbin Li,[a] Dongmei Dai,[a] Fengtao Zhang,[b] Hongli Zou,[a] Xiaoxiao Yang,[a] Yahui Ji,[a] Bao Li,*[a] Xianjun Wei*[a]*

[a] Collaborative Innovation Center of Henan Province for Green Manufacturing of Fine Chemicals, Key Laboratory of Green Chemical Media and Reactions (Ministry of Education), School of Chemistry and Chemical Engineering, Henan Normal University, Xinxiang Henan 453007, P. R. China.

E-mail: tom-jswei@outlook.com; libao@htu.edu.cn; xianjunwei@htu.cn

[b]Beijing National Laboratory for Molecular Sciences, Key Laboratory of Colloid, Interface and Thermodynamics, Institute of Chemistry, Chinese Academy of Sciences, Beijing, 100190, P. R. China.

This PDF file includes:

Materials and Methods, **Figure S1** to **S11**, **Tables S1** to **S4**, References.

1. Materials and Methods

1.1 Materials

Windmill palm buds (WPBs) were harvested from parks in Xinxiang region (Henan province, China). WPB samples were sorted, cleaned thoroughly, dried at 80 °C in the oven and smashed for further use. Hydrochloric acid (HCl, 36 wt.%, AR) and potassium hydroxide (KOH, 85 wt. %, AR) were purchased from Aladdin Reagent (Shanghai) Co., Ltd, China, and all chemicals were used as received.

1.2 Preparation of HPCs derived from WPBs

A typical preparation process included two stages: carbonization and activation. In the carbonization stage, the WPB powder was carbonized at 500 °C for 2 h at a 5 °C min^{-1} heating rate from room temperature in a tubular furnace under a nitrogen atmosphere. In the activation stage, pre-carbonized products were mixed with KOH in a mass ratio of 4 followed by activated at set temperature (such as 700 or 800 °C) for 2 h at a heating rate of 10 °C min^{-1} in N_2 atmosphere, and cooled to room temperature in the tubular furnace. The carbonized products were immersed into 2 mol L^{-1} HCl solutions, filtered and followed washed by distilled water until the filtrate was neutral, then dried in an oven at 75 °C and the hierarchical porous carbons (HPCs) were obtained. The resulted HPCs were marked as AWPB-700 and AWPB-800 (activated WPB based carbon), where the number such as 700 or 800 indicates activation temperature, respectively. WPB-700, which was derived from **WPBs** calcined at 700 °C without adding KOH, expresses a sample used as to compare its properties with that of AWPB-700. **Figure. 1** (manuscript) shows the schematic illustration about the preparation of HPCs using WPBs as the precursor.

1.3 Morphological and structural characterization

FE-SEM (field emission scanning electron microscope, Zeiss Supra 40 FE-SEM) and TEM (transmission electron microscopy, JEOL JEM-2100 microscope) technologies were used to characterize the morphology and structure of the samples. The N_2 adsorption/desorption properties of the products were tested on a Quantachrome Automated IQ2 surface and pore size analyzer. Surface area was calculated according to multi-point BET (Brunauer-Emmett-Teller)

theory, and micropore or mesopore surface area was valued by t-plot method. Pore size distribution was determined by non-local density functional theory (NLDFT) methods. CO_2 adsorption tests were conducted at 298/273 K, and related micro pore distribution curves were calculated by NLDFT model. X-ray photoelectron spectroscopy (XPS, ESCALAB 250 spectrometer, 300.0 eV, Al Ka radiation) and fourier transform infrared spectroscopy (FTIR, Perkin Elmer Avatar 360 E.S.P using KBr pellets) were used to determine the elemental composition. Moreover, crystalline structure data and Raman spectra were collected from an X-ray diffractometer (XRD, Bruker D8 X-ray diffractometer, 0.1541 nm, Cu-Kα radiation) and a Renishaw Raman spectrometer with 532 nm excitation wavelength. The contact angle measurements were performed on a contact angle tester (KRüSS DSA25).

1.4 Electrochemical measurements

Cyclic voltammograms (CVs), electrochemical impedance spectra (EIS) and galvanostatic charge/discharge (GCD) measurements were performed to evaluate the electrochemical performances of samples in three- or two-electrode system using 1 mol L^{-1} H_2SO_4 aqueous solution at room temperature. In three-electrode measurement system, Hg/Hg_2SO_4 (in H_2SO_4 solution) was used as reference electrode, and stainless steel grid was chose as the counter one. The used working electrode was assembled by HPC active material, binder, conductor and current collector. A typical manufacturing process of the working electrode was as follows: HPCs were blended with acetylene black and polytetrafluoroethylene based on the weight ratio of 75:20:5, and the resulted mixture was fully grinded into a paste, which was forcibly and uniformly coated onto the current collector (active material loading of about 1.1 mg, and coating area of about 1 cm^2), then dried in an oven at 80 °C for 24 h. Specific capacitance, energy density or power density was calculated from GCD data. Two carefully selected electrodes with the same active material loading were used to assemble a series of symmetric supercapacitor devices to measure GCD and CVs. CVs, EIS and GCD were recorded on electrochemical workstation (CHI660E, CHI760B, Chenhua, Shanghai, China), or on potentiostat/galvanostat (CT2001A, Land, Wuhan, China).

The specific capacitance, energy density and power density value were calculated from GCD data according to our recent reports. [S1]

2. Figures and Tables

Table S1. Porosity properties (according to N_2 adsorption/desorption measurements) and specific capacitance of samples in 1 mol L^{-1} of H_2SO_4 at current density of 1 A g^{-1}.

Samples	S_{BET} ($m^2 g^{-1}$)	S_{micr} ($m^2 g^{-1}$)	S_{exter} ($m^2 g^{-1}$)	V_{tot} ($cm^3 g^{-1}$)	V_{micr} ($cm^3 g^{-1}$)	$D_{average}$ (nm)	C_g (F g^{-1})
AWPB-700	3156.0	2835.0	321.0	1.616	1.295	2.048	562
AWPB-800	3084.0	2432.0	652.0	1.763	1.186	2.287	367
WPB-700	8.0	-	8.0	0.030	-	1.520	41.9

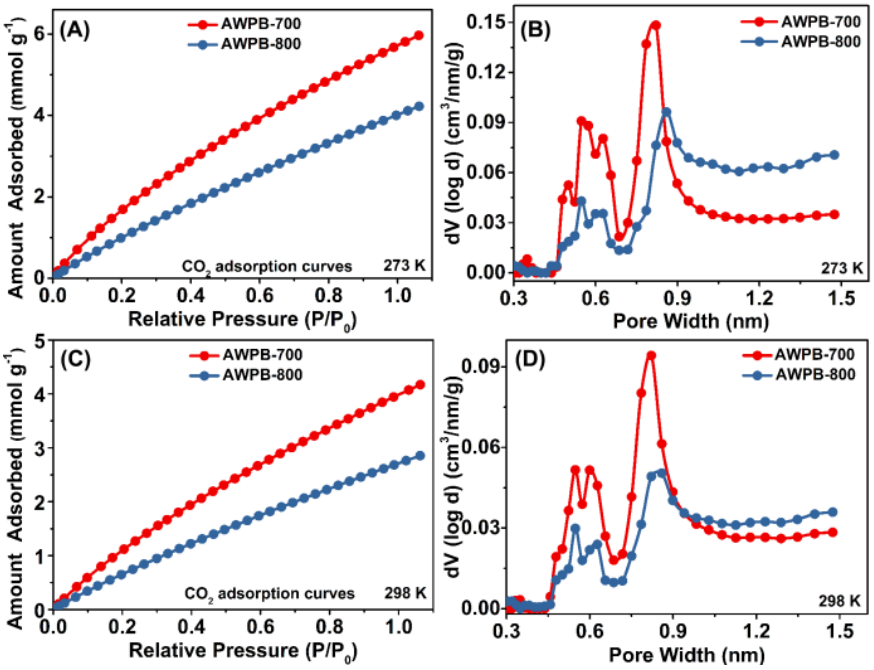

Figure S1. The CO_2 adsorption isotherms at (A) 273 K and (C) 298 K temperature for AWPB based carbons; the corresponding micro pore distribution curves calculated from NLDFT model at (B) 273 K and (D) 298 K.

CO_2 adsorption measurements were also conducted to evaluate the microporous structures more precisely. CO_2 adsorption isotherms on the AWPB based carbons at ambient pressure and 273 K and 298 K are illustrated in **Figure S1** A and C. It can be seen that the trend of CO_2 adsorption at 273 K and 298 K are quite similar. And the absorbed amounts of CO_2 decrease with temperature, demonstrating a physical adsorption characteristic. Micro pore size distribution (PSD) curves (Shown as **Figure S1** B and D) tested by CO_2 adsorption method suggests the microporous structures of two samples are similar (consistent with PSD curves tested by

nitrogen adsorption, **Figure 2** D, manuscript). And these results are consistent with nitrogen adsorption measurements.

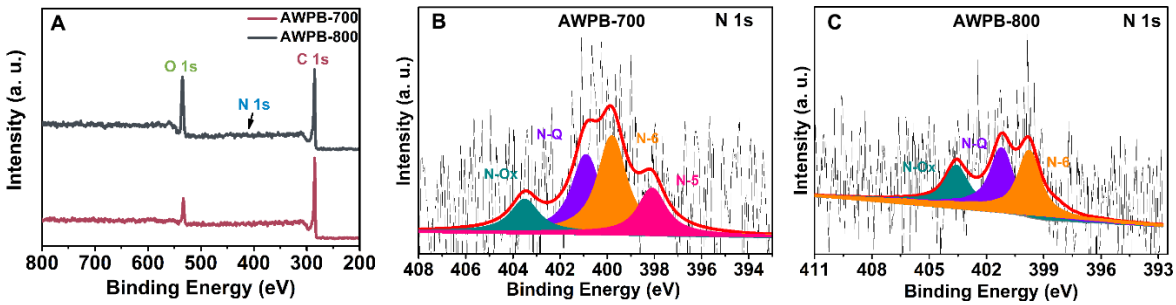

Figure. S2 (A) XPS survey spectra of AWPB-700 and AWPB-800, High-resolution XPS of N 1s of (B) AWPB-700 and (C) AWPB-800.

Table S2. Surface atomic compositions of AWPB-700/800 derived from XPS results.

Samples	Species concentration (%)			N1s (%)				O1s (%)			
	C 1s	N 1s	O 1s	N-6	N-5	N-Ox	N-Q	C=O	C-OH	C-O-C	COOH
AWPB-700	88.43	0.32	11.25	0.06	0.12	0.10	0.04	0.31	5.10	4.24	1.60
AWPB-800	83.93	0.40	15.67	0.01	0.15	0.15	0.09	0.70	6.45	5.43	3.10

Note: The difference of oxygen species concentration certainly exists between the two samples. However, as for the oxygen species (like C-OH and C=O groups) which can bring faradic reactions in acid electrolyte, and their concentration differences are not obvious (C=O and C-OH concentrations in AWPB-800 are only 0.39% and 1.35 % higher than that of in AWPB-700, respectively).

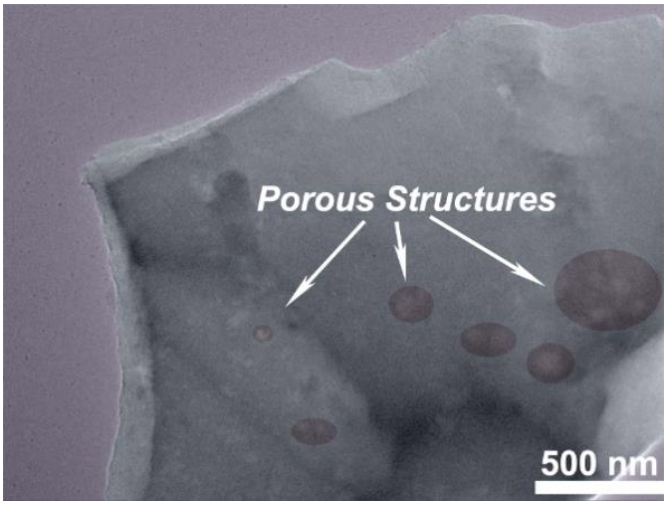

Figure. S3 TEM images of AWPB-700 (optimal sample).

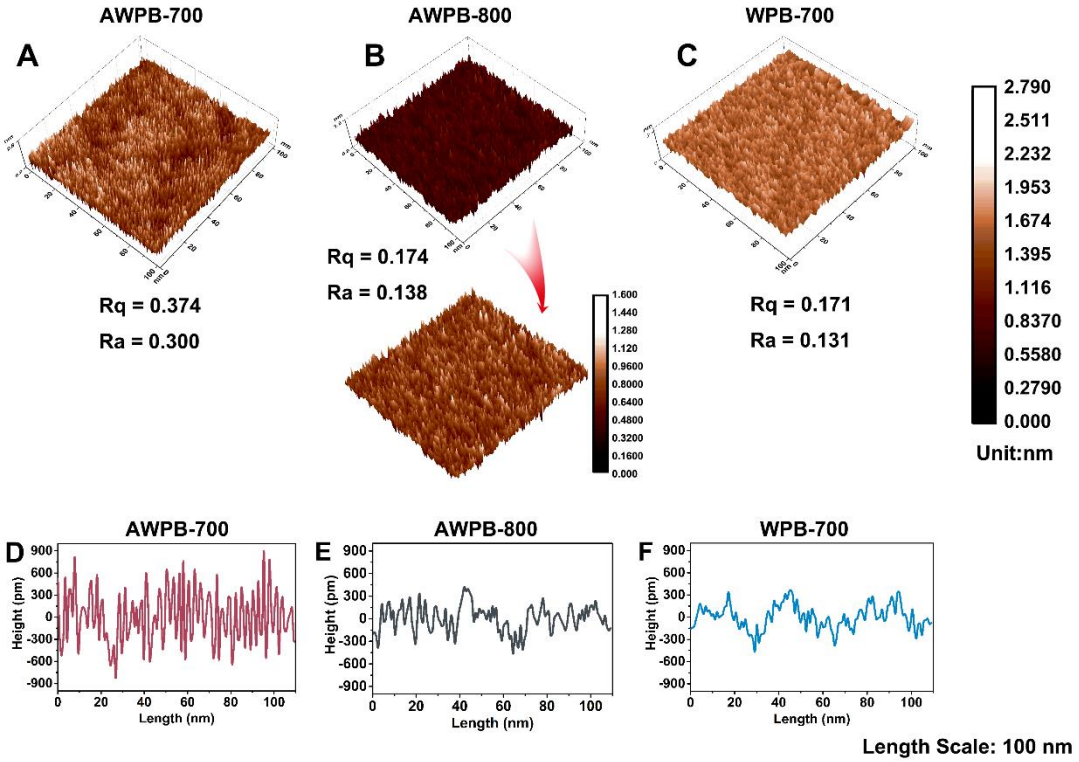

Figure. S4 AFM images of (A) AWPB-700, (B) AWPB-800 and (C) WPB-700. Typical surface line profiles of (D) AWPB-700, (E) AWPB-800 and (F) WPB-700 represent the roughness. Length scale: 100 nm.

Note: Ra and Rq are amplitude parameters to characterize the surface based on the vertical deviations of the roughness profile from the mean line. For Ra, it presents arithmetical mean deviation of the assessed profile. More specifically, Ra is the arithmetic average value of filtered roughness profile determined from deviations about the center line within the evaluation length. And parameter Rq is the root mean squared, which is defined as the square root of the mean square.

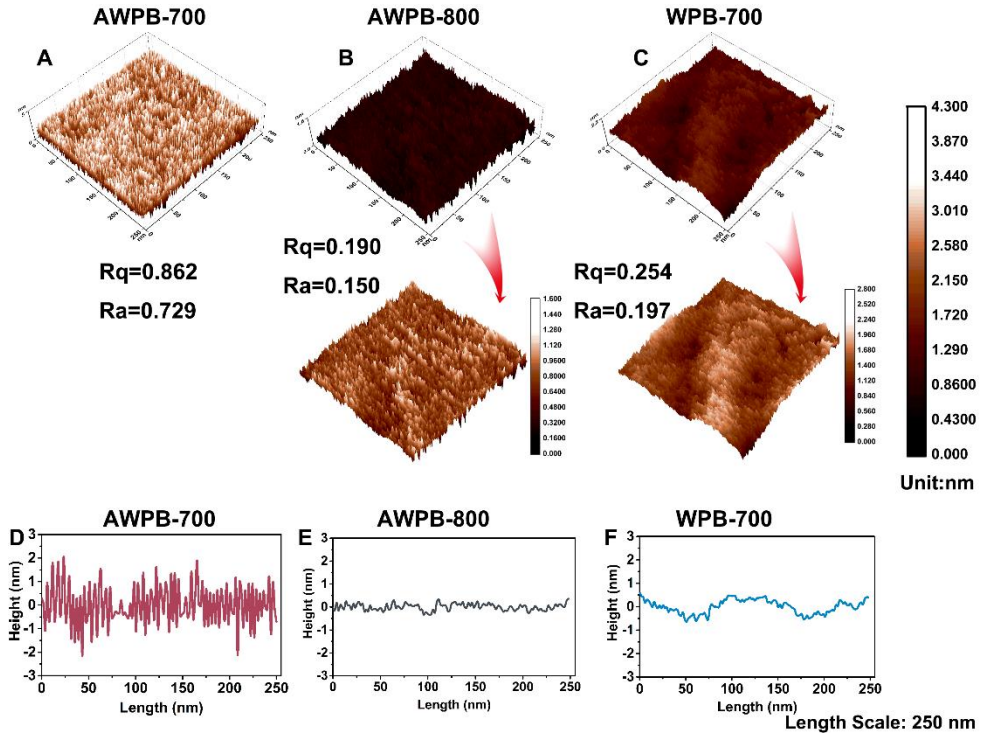

Figure. S5 AFM images of (A) AWPB-700, (B) AWPB-800 and (C) WPB-700. Typical surface line profiles of (D) AWPB-700, (E) AWPB-800 and (F) WPB-700 represent the roughness. Length scale: 250 nm.

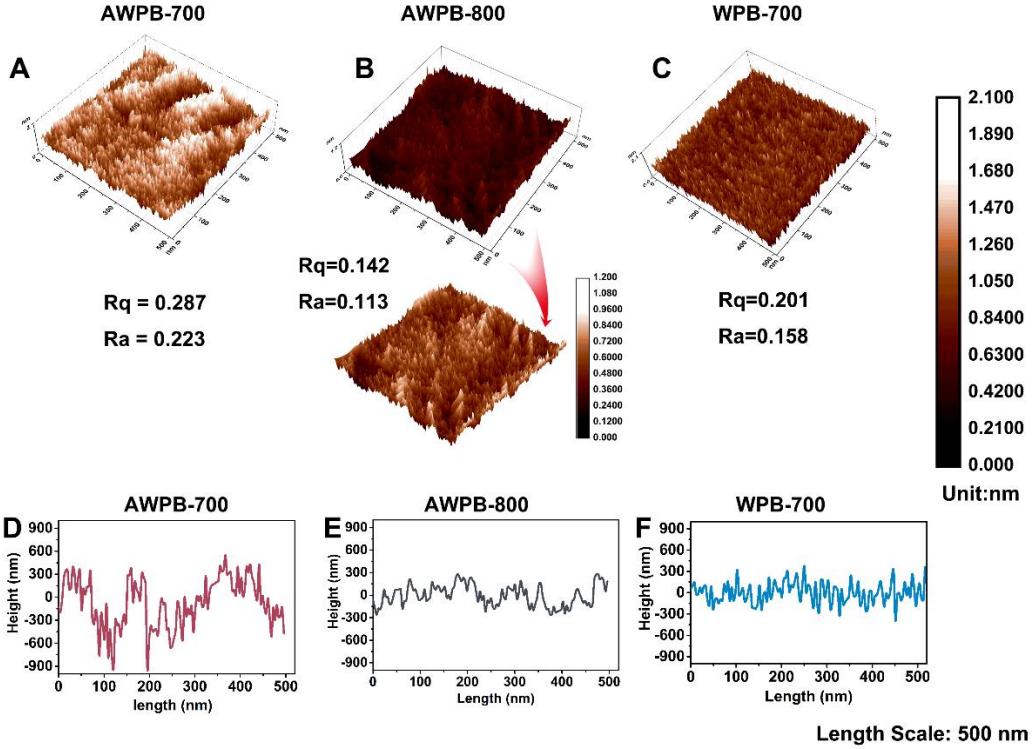

Figure. S6 AFM images of (A) AWPB-700, (B) AWPB-800 and (C) WPB-700. Typical surface line profiles of (D) AWPB-700, (E) AWPB-800 and (F) WPB-700 represent the roughness. Length scale: 500 nm.

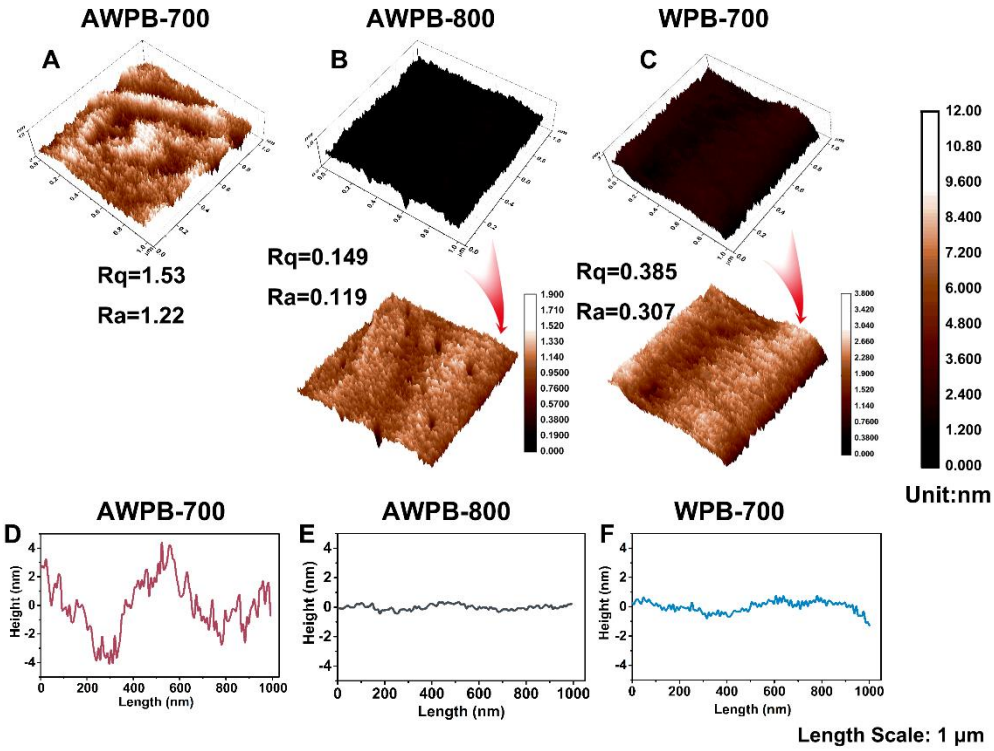

Figure. S7 AFM images of (A) AWPB-700, (B) AWPB-800 and (C) WPB-700. Typical surface line profiles of (D) AWPB-700, (E) AWPB-800 and (F) WPB-700 represent the roughness. Length scale: 1000 nm.

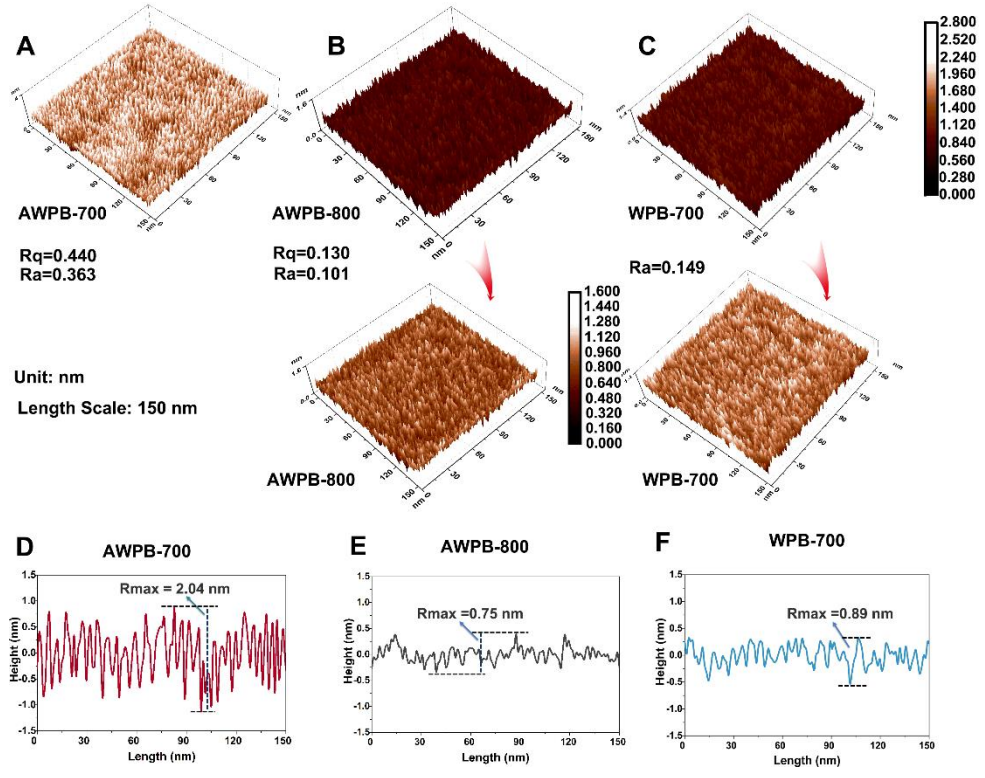

Figure. S8 AFM images of (A) AWPB-700, (B) AWPB-800 and (C) WPB-700 from another

batch. Surface line profiles of (D) AWPB-700, (E) AWPB-800 and (F) WPB-700 represent the roughness. Length scale: 150 nm.

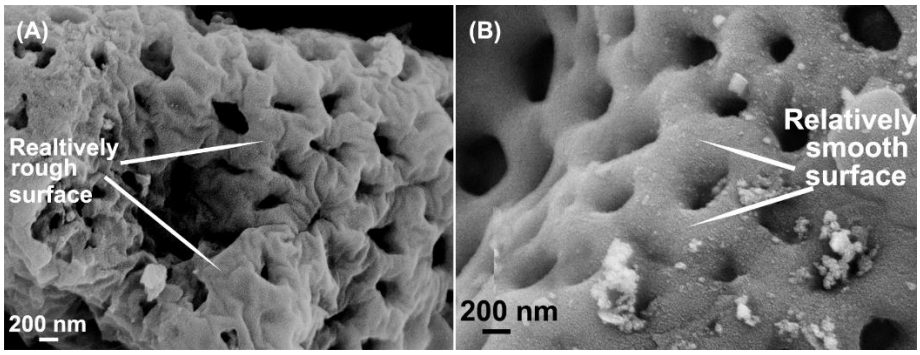

Figure S9. SEM images of (A) AWPB-700 (optimal sample) and (B) AWPB-800 from another batch.

Repeated experiments through samples from different batch were employed to evaluate the repeatability of above surface roughness measurements. Amounts of AFM and FESEM data from another batch of samples are used to support above views and conclusions (**Figure S4-7**, SI). Taking AFM measurements as examples, two samples from different batches, related roughness value and AFM images are shown as **Figure S8**.

Although at a much smaller length scale, related results can also reflect the difference in surface roughness, which are consistent with data shown in **Figure 4** and **Figure S4-7**. Among that, R_q value of AWPB-800 is only 0.130 nm, and the corresponding R_{max} (difference in height between the highest and lowest points on the cross-sectional profile relative to the center line (not the roughness curve) over the length of the profile, **Figure S8** E) just can reach 0.75 nm. In contrast, R_q value of AWPB-700 can reach 0.440 nm, and the corresponding R_{max} can reach 2.04 nm (**Figure S8** D). Similarly, another type of roughness value (R_a) for wrinkles, which is the arithmetic mean of the absolute values of the surface height deviations surveyed from the mean plane in the selected area, sharply decreases from 1.22 nm (AWPB-700) to 0.119 nm (AWPB-800) with higher activation temperature. Without chemical activation, the blank sample, WPB-700, also shows a low surface roughness. Thus, discrepancy of surface roughness between

AWPB-700 and 800 can be reflected by specific data.

SEM images shown as **Figure S9** are consistent with previous results in manuscript (Figure 3). Despite the two samples have similar micromorphology, higher surface roughness makes the sample AWPB-700 be easily distinguished. The surface of AWPB-700 exhibits more folds and tiny wrinkles (**Figure S9** A), while relatively smooth surface is the feature of AWPB-800 (**Figure S9** B).

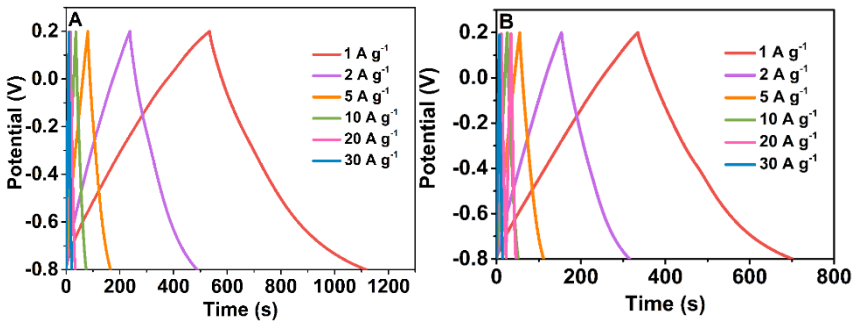

Figure. S10 Charging-discharging curves of (A) AWPB-700 and (B) AWPB-800 at different current densities in three-electrode system.

Table S3. Specific surface area (SSA), total pore volume (V_{tot}), hetero-element content and specific capacitances (C_g, aqueous condition, three-electrode system) of optimal sample in comparison with porous carbon based supercapacitors materials in literatures.

Sample	SSA ($m^2 g^{-1}$)	V_{tot} ($cm^3 g^{-1}$)	Hetero-Element Content (at.%)	C_g, Current Density	Literatures
AWPB-700	**3156**	**1.62**	**11.57**	**562 F g^{-1}, 1 A g^{-1}**	**This Work**
AWPB-800	3084	1.76	16.07	367 F g^{-1}, 1 A g^{-1}	This work
[a]Mushroom based carbon	2988	1.76	8.9	306 F g^{-1}, 1 A g^{-1}	Ref. [S2]
[a]Pomelo peel based carbon	2725	1.28	11.4	342 F g^{-1}, 0.2 A g^{-1}	Ref. [S3]
[a]Celtuce leaves based carbon	3239	1.88	4.31	421 F g^{-1}, 0.5 A g^{-1}	Ref. [S4]
[b]Polyacrylonitrile-based carbon	3751	2.48	12	448 F g^{-1}, 0.5 A g^{-1}	Ref. [S5]
[b]Hypercrosslinked organic porous polymer based carbon (phenyltrimethylsilane as monomer)	3101	1.84	11.33	355 F g^{-1}, 0.5 A g^{-1}	Ref. [S6]
[b]PANI-PVA based carbon	2675	1.055	18.82	497 F g^{-1}, 1 A g^{-1}	Ref. [S7]
[c]AC/Graphene aerogels	2400	1.15	-	294 F g^{-1}, 0.05 A g^{-1}	Ref. [S8]
[c] Nano porous Graphene Sheets	2396	1.6	3.5	282 F g^{-1}, 0.5 A g^{-1}	Ref. [S9]
[d]EDTA-2K	3179	3.4	14.7	268 F g^{-1}, 5 mV s^{-1}	Ref. [S10]

Note: Precursors of porous carbon are [a]bio-materials, [b]polymer, [c]graphene and [d]organic salt.

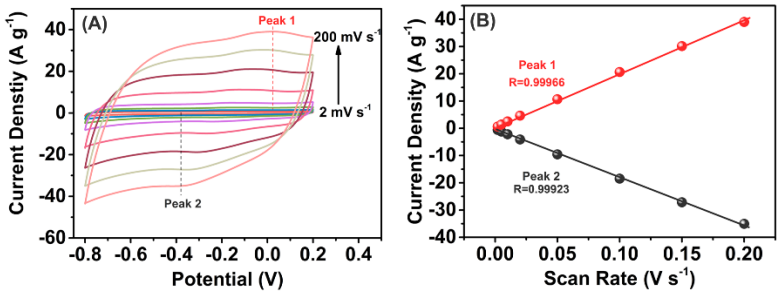

Figure S11. (A) CV curves of optimal sample (AWPB-700) at different scan rates, and (B) the relationship between current density and scan rate (v^{1})

Table S4. Parameters of the equivalent circuit (EIS) for different carbon materials

Sample	[a]R_s (Ω)	[b]R_{ct} (Ω)	[c]R_p (Ω)	R_{total} (Ω)
AWPB-700	1.23	0.67	1.18	3.08
AWPB-800	1.39	0.66	1.38	3.43

[a] *R_s, ion migration resistance in the bulk solution.*

[b] *R_{ct}, internal contact resistance of the electrode.*

[c] *R_p, equivalent distributed resistance for ion diffusion in the micropores*

References

S1. Wei, X.; Wei, J.-S.; Li, Y.; Zou, H., Robust Hierarchically Interconnected Porous Carbons Derived from Discarded Rhus Typhina Fruits for Ultrahigh Capacitive Performance Supercapacitors. *J. Power Sources* **2019,** *414*, 13-23.

S2. Cheng, P.; Gao, S.; Zang, P.; Yang, X.; Bai, Y.; Xu, H.; Liu, Z.; Lei, Z., Hierarchically Porous Carbon by Activation of Shiitake Mushroom for Capacitive Energy Storage. *Carbon* **2015,** *93*, 315-324.

S3. Liang, Q.; Ye, L.; Huang, Z.-H.; Xu, Q.; Bai, Y.; Kang, F.; Yang, Q.-H., A Honeycomb-like Porous Carbon Derived from Pomelo Peel for Use in High-performance Supercapacitors. *Nanoscale* **2014,** *6*, 13831-13837.

S4. Wang, R.; Wang, P.; Yan, X.; Lang, J.; Peng, C.; Xue, Q., Promising Porous Carbon Derived from Celtuce Leaves with Outstanding Supercapacitance and CO_2 Capture Performance. *ACS Appl. Mater. Interfaces* **2012,** *4*, 5800-5806.

S5. Li, Y.; Liang, Y.; Hu, H.; Dong, H.; Zheng, M.; Xiao, Y.; Liu, Y., KNO_3-mediated Synthesis of High-surface-area Polyacrylonitrile-based Carbon Material for Exceptional Supercapacitors. *Carbon* **2019,** *152*, 120-127.

S6. Zhang, C.; Kong, R.; Wang, X.; Xu, Y.; Wang, F.; Ren, W.; Wang, Y.; Su, F.; Jiang, J.-X., Porous Carbons Derived from Hypercross Linked Porous Polymers for Gas Adsorption and Energy Storage. *Carbon* **2017,** *114*, 608-618.

S7. Wei, X.; Zou, H.; Gao, S., Chemical Crosslinking Engineered Nitrogen-doped Carbon Aerogels from Polyaniline-boric Acid-polyvinyl Alcohol Gels for High-performance Electrochemical Capacitors. *Carbon* **2017,** *123*, 471-480.

S8. Zhu, Q.; Ma, L.; Wang, H.; Jia, M.; Guan, Y.; Xu, B., Activated Carbon / Graphene Hybrid Aerogels as Electrode Materials for High Performance Supercapacitors. *ChemistrySelect* **2017,** *2*, 4456-4461.

S9. Nanaji, K.; Upadhyayula, V.; Rao, T. N.; Anandan, S., Robust, Environmentally Benign Synthesis of Nanoporous Graphene Sheets from Biowaste for Ultrafast Supercapacitor Application. *ACS Sustainable Chem. Eng.* **2018,** *7*, 2516-2529.

S10. Zhang, Y.; Ma, Q.; Li, H.; Yang, Y.-W.; Luo, J., Robust Production of Ultrahigh Surface Area Carbon Sheets for Energy Storage. *Small* **2018,** *14*, 1800133.